Direct coupling of continuum and kinetic Monte Carlo models for multiscale simulation of electrochemical systems

Fridolin Röder [a,b], Richard D. Braatz [c], Ulrike Krewer [a,b,*]

[a] *Institute of Energy and Process Systems Engineering, TU Braunschweig, Franz-Liszt-Strasse 35, Braunschweig 38106, Germany*
[b] *Battery LabFactory Braunschweig, TU Braunschweig, Langer Kamp 19, Braunschweig 38106, Germany*
[c] *Massachusetts Institute of Technology, 77 Massachusetts Avenue, Cambridge, MA 02319, USA*

ARTICLE INFO

ABSTRACT

Electrochemical systems include atomistic processes at electrochemical interfaces and macroscopic transport processes, which can be modeled using kinetic Monte Carlo (kMC) simulation and continuum equations, respectively. Multiparadigm algorithms are applied to directly couple such models to study multiscale interactions. This article compares different algorithms for an example problem. Results quantify the effect of computational cost and numerical accuracy by the choice of algorithm and its configuration. The stochastic fluctuations of kMC simulations as well as sequential data exchange between the models generate errors in coupled simulations. Measures to reduce stochastic fluctuations or revise exchanged data can be either highly successful or futile, depending on the dominant cause of the error. Hence, we strongly advise to identify the different causes of errors and their mechanics when selecting a coupling algorithm or optimizing its configuration. This article provides various algorithms and suggestions for their configuration to enable efficient and robust multiscale simulations.

1. Introduction

Modeling and simulation have long been applied to the operation, diagnosis, and optimization of electrochemical systems and processes (e.g., Ramadesigan et al., 2012 and citations therein). Most applications construct models via a top-down approach, in which a description of the technically relevant phenomena is based on as little physical detail as needed to describe the system's performance. The demand for computational efficiency often leads to the application of simplified physical or phenomenological homogenized continuum models. However, for many systems, in particular those containing active surfaces, their behavior is determined by complex mechanisms that occur at the atomistic scale, such as electrochemical surface degradation in batteries or fuel cells. In order to facilitate a knowledge-driven optimization of such systems, atomistic effects need to be included in macroscopic models, which leads to an increasing need for multiscale simulations (Braatz et al., 2008). Simulation techniques applicable for small length scales, such as the kinetic Monte Carlo (kMC) method, are often of a stochastic nature and cannot be simulated for the larger length and time scales describable by continuum models. Therefore, multiparadigm approaches are used to bridge those scales. The coupling of scales can be realized directly or indirectly (Franco, 2013). Only direct coupling allows for the investigation of the interaction of the models and phenomena between the scales. Direct coupling of different simulation paradigms is challenging due to the fundamentally different representation of physical processes at different scales. Coupling algorithms need to be further developed in order to improve accuracy and computational efficiency (Salciccioli et al., 2011). Better algorithms will help to further spread the application of those techniques, which promise to lift electrochemical modeling to a more advanced and accurate stage for the description of physical processes. The narrowing of the gap between engineering and computational chemistry is important for electrochemical systems in particular, and heterogeneous catalysis in general (Kalz et al., 2016).

In this article, we investigate methods for the direct coupling of kMC and continuum models based on differential equations. KMC has been shown to be a useful tool to investigate surface chemistry for many years (Pal and Landau, 1994). An excellent overview on concepts, status, and challenges of applying first-principles KMC to reactions at surfaces is given in Reuter (2011). In electrochemistry, for instance, kMC has been applied to investigate CO electro oxidation (Andreaus and Eikerling, 2007), copper electrodeposition (Drews et al., 2006), fuel cells (Pornprasertsuk et al., 2007), and

* Corresponding author at: Institute of Energy and Process Systems Engineering, TU Braunschweig, Franz-Liszt-Str. 35, 38106 Braunschweig, Germany.

E-mail addresses: f.roeder@tu-braunschweig.de (F. Röder), braatz@mit.edu (R.D. Braatz), u.krewer@tu-braunschweig.de (U. Krewer).

List of symbols

Latin letters

a_s	specific surface area, m^{-1}
$\bar{A}$	amplitude, $A\ m^{-2}$
c	concentration, $mol\ m^{-3}$ or $mol\ m^{-2}$
C^{DL}	double layer capacitance, $F\ m^{-2}$
C^0	standard state concentration, $mol\ m^{-3}$
E^A	activation energy, $J\ mol^{-1}$
E^M	estimation of mean value
E^S	estimation of the standard deviation
f	frequency, s^{-1}
F	Faraday constant, $A\ s\ mol^{-1}$
I	applied current, $A\ m^{-2}$
J	an elementary process, –
Ψ^j	boolean of elementary process j, –
k	rate constant, s^{-1}
k^f	forward reaction rate constant, [s, mol, m]
k^b	backward reaction rate constant, [s, mol, m]
L	a lattice site, –
M_s^p	mean value of output parameter sample p of sequence s
M_e^{p*}	mean value of output parameter sample p of iteration e
n^l	total number of lattice sites in kMC instance, –
n_j	total number of elementary processes, –
n_x^l	number of lattice sites in x direction in kMC instance, –
n_y^l	number of lattice sites in x direction in kMC instance, –
n^{par}	number of parallel kMC instances, –
n^{seq}	number of sequences, –
N_s	site density, m^{-2}
o_s	site occupancy number, mol^{-1}
p	kMC output
q	reaction flux, $mol\ m^{-2}\ s^{-1}$
R	ideal gas constant, $J\ mol^{-1}\ K^{-1}$
S_s^p	standard deviation of the mean value M of sequence s
S_e^{p*}	standard deviation of the mean value M of iteration e
t	time, s
T	temperature, K

Greek letters

β	symmetry factor, –
$\Delta\Phi$	drop of electrical potential at the interface, V
ΔG^0	standard state Gibbs free energy, $J\ mol^{-1}$
ΔL	size of lattice site, m
Δt	step time length, s
Γ	microscopic rate, s^{-1}
ι	a kMC step, –
κ	smoothing factor, –
ϑ	lattice site state, –
ς	a sequence, –
θ	surface fraction, –
ζ	uniform distributed random number, –

Indices

ads	adsorption site
E	electrolyte
B	species B
A^+	charges species A
C	species C
V	vacancy
l	lattice site index
i	kMC step index
s	sequence index
j	elementary process index
v	kMC instance index
e	iteration index
par	parallel instance of the kMC model
seq	sequence
tot	total
kMC	kinetic Monte Carlo
end	end of simulation
error	error compared to continuum solution
continuum	continuum solution
MPA	solution using algorithm MPA

batteries (Blanquer et al., 2016; Methekar et al., 2011). In contrast to continuum models, kMC allows the study of lateral stochastic interactions of molecules on surfaces at the atomistic scale (Jahnke et al., 2016).

KMC models can be coupled with continuum models in a multiparadigm model (Braatz et al., 2008; Franco, 2013; Jahnke et al., 2016). The importance, perspectives, and challenges of such coupled models have been outlined by various researchers, e.g., Braatz et al. (2008); Franco (2013); Jahnke et al. (2016); Salciccioli et al. (2011) and Ricardez-Sandoval (2011). Multiparadigm algorithms have been applied to study the agglomeration of particles in reactors by coupling computational fluid dynamics (CFD) with Monte Carlo methods (Madec et al., 2001), CO oxidation in a catalytic reactor by coupling CFD and first principal kMC (Matera et al., 2014), in the additive-mediated electrodeposition of copper (Zheng et al., 2008), and to fuel cells and other energy storage systems (Quiroga and Franco, 2015; Quiroga et al., 2016). In the field of batteries, mulitparadigm approaches have been used to study the formation of the solid electrolyte interface on negative electrodes in lithium-ion batteries (Methekar et al., 2011; Röder et al., 2017). Further, coupling algorithms are also applied in several multiphysics simulation, such as coupling of thermal and electrochemical models for simulation of batteries (Lin et al., 2018) or coupling of CFD and reaction kinetic models for simulation of reformers (Goldin et al., 2009).

In general, direct coupling – also called hybrid or heterogeneous-homogeneous coupling – and indirect coupling can be distinguished. Direct coupling includes a frequent interaction of continuum model and kMC model during simulation (Franco, 2013). Designing a numerically stable and accurate direct multiparadigm algorithm is challenging, and so an indirect coupling strategy is preferred if such a formulation can be derived that sufficiently captures the underlying coupled phenomena. Some multiscale systems, however, need direct coupling to accurately describe their behavior (Braatz et al., 2008). Direct coupling separates the simulation into time intervals where the kMC and the continuum model are solved in sequence or in parallel (Ricardez-Sandoval, 2011). Both algorithms can be iterated multiple times within each time interval convergence to self-consistent solutions between the models (Vlachos, 1997). Further, filtering techniques are often applied to reduce fluctuations of the kMC output (Braatz et al., 2006; Drews et al., 2004). All aspects have considerable impact on accuracy and computational cost of the simulation, which is rarely addressed. Theoretical approaches are available (Rusli et al., 2004; To and Li, 2005; Weinan et al., 2003), but no comprehensive comparison is available between different strategies and their impact on accuracy and computational cost.

Table 1

Reactions and adsorption/desorption processes I-IV, with continuum processes and their rate constants k and the processes j as considered in the kMC model with their microscopic rates Γ.

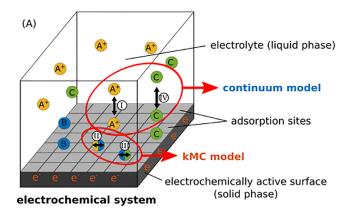| Nb.	Continuum process	j	kMC process
I	$A^+(E) + V(ads) \underset{k_I^b}{\overset{k_I^f}{\rightleftharpoons}} A^+(ads)$	–	–
		–	–
II	$A^+(ads) + e^-(el) \underset{k_{II}^b}{\overset{k_{II}^f}{\rightleftharpoons}} B(ads)$	1	$A^+(ads) + e^-(el) \xrightarrow{\Gamma_i^{I1}} B(ads)$
		2	$B(ads) \xrightarrow{\Gamma_i^{I2}} A^+(ads) + e^-(el)$
III	$B(ads) \underset{k_{III}^b}{\overset{k_{III}^f}{\rightleftharpoons}} C(ads)$	3	$B(ads) \xrightarrow{\Gamma_i^{I3}} C(ads)$
		4	$C(ads) \xrightarrow{\Gamma_i^{I4}} B(ads)$
IV	$C(E) + V(ads) \underset{k_{IV}^b}{\overset{k_{IV}^f}{\rightleftharpoons}} C(ads)$	–	–
		–	–

The scope of this article is to give the first systematic design, evaluation and comparison of algorithms for direct coupling of kMC with continuum models for electrochemical problems. The focus is on electrochemical interfaces, which arise in many systems of scientific and engineering interest. To benchmark the performance of the algorithms, a simple example problem is defined with sequential reactions with only first-order reaction kinetics including an electrochemical reaction step. By excluding heterogeneous processes, i.e. atom to atom interaction, the problem can be accurately solved using mean field approximation in pure continuum codes, which enables the evaluation of the accuracy of the multiparadigm simulations. We aim to provide an introduction to direct multiparadigm algorithms applicable to surface degradation problems in electrochemical engineering. Further, we show the impact of grid size, time step length, and smoothing of fluctuations on the performance, i.e. computational cost and accuracy, of the algorithms.
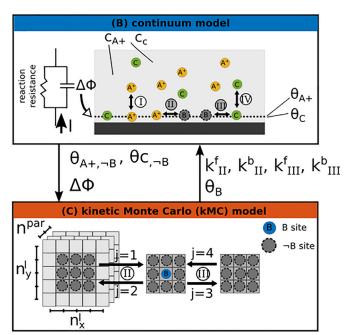
2. Computational details

2.1. Example problem

For the purpose of evaluating multiscale modeling algorithms, a simple example problem is introduced, which includes a mechanism of two consecutive reactions of first order, without interaction of the species on the surface. The mechanism is illustrated in Fig. 1(A) and the considered processes are given in Table 1. Process I is adsorption of species A^+ from the liquid phase, i.e. the electrolyte, to the surface. Process II is the electrochemical reaction of species A^+ to species B. Process III is the subsequent chemical reaction of species B to species C. Finally, Process IV is the desorption of species C from the surface. All processes are reversible. The presented example problem does not include any atom to atom interaction and can thus also be solved exactly by a pure continuum code, allowing the validation of the multiparadigm code and benchmark of the different multiparadigm algorithms. This holds not only for first order reaction, but also for second order reactions in the absence of lateral interactions.

With the here presented multiparadigm approach, a continuum model composed of ordinary differential equations, and an atomistic model using the kMC method, are directly coupled. The thermodynamics and kinetics of each process in each model are detailed below. With this work we suggest, that only the processes of particular interest or clearly heterogeneous nature should be modeled on an atomistic scale (e.g., Zheng et al., 2008). All other processes, which can be sufficiently accurately approximated by mean field approaches, should preferably be solved by the much faster

Fig. 1. Example of the electrochemical system (A) and illustration of the multiparadigm model including the continuum model (B) and the kMC model (C). Species and processes not addressed in a model are colored in gray.
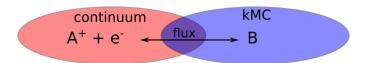

Fig. 2. Illustration of the interface between kMC and continuum models.

continuum codes. The boundary between models is defined between educts and products of a process, which is illustrated in Fig. 2 for process II. Species A^+ and e^- are considered by the continuum model and species B is considered by the kMC model. The models are coupled by synchronization of the fluxes, e.g. the flux of process II. In general, the boundary between continuum and kMC model can be flexibly defined at every considered process. The choice will depend on the investigated problem.

In the following, first the continuum and the kMC model is provided. Then, the sequence concept and the multiparadigm algorithms for coupling of those models are introduced. Finally, the approach to quantify simulation errors and the investigated simulation scenario are given.

2.2. Continuum model

The scope of the continuum model is illustrated in Fig. 1(B). It features changes of electrical potential, $\Delta\Phi$, at the interface, changes of concentrations of species A^+ and C, $c_{A^+(E)}$ and $c_{C(E)}$, within the electrolyte, and changes of surface fractions of species A^+ and C, $\theta_{A^+(ads)}$ and $\theta_{C(ads)}$, on the adsorption site. Surface fraction of B, $\theta_{B(ads)}$, is an input parameter provided by the kMC model. Further, the model covers expressions for processes I-IV, as illustrated in Fig. 1(B). While processes I and IV are independent of the kMC model, processes II and III are synchronized with the kMC model by adapting the forward and backward reaction rate constants of reactions II and III, namely k_{II}^f, k_{II}^b, k_{III}^f, k_{III}^b. It is noted that instead of passing reaction rate constants, reaction fluxes can also be passed from the kMC to the continuum model. However, passing rate constants yields more numerically stable codes, as discussed below. In the following, the equations of the continuum model are given.

The charge balance is included as

$$C^{DL}\frac{d\Delta\Phi}{dt} = I - q_{II}F \tag{1}$$

with applied electrical current I, surface flux of the electrochemical reaction II, q_{II}, double layer capacitance C^{DL} and Faraday constant F. Balance equations for surface fraction of species A^+ and C are given as

$$\frac{N_s}{o_s}\frac{d\theta_{A^+(ads)}}{dt} = q_I - q_{II} \tag{2}$$

and

$$\frac{N_s}{o_s}\frac{d\theta_{C(ads)}}{dt} = q_{III} + q_{IV}, \tag{3}$$

respectively, using site density N_s, site-occupancy number o_s and fluxes q of processes I–IV. Balance equations for concentrations of A^+ and C within the electrolyte are included as

$$\frac{1}{a_s}\frac{dc_{A^+(E)}}{dt} = q_I \tag{4}$$

and

$$\frac{1}{a_s}\frac{dc_{C(E)}}{dt} = q_{IV}, \tag{5}$$

respectively, using specific surface area a_s. Fluxes q of processes I-IV are provided by

$$\frac{o_s}{N_s}q_I = k_I^f\theta_V\frac{c_{A^+(E)}}{C^0_{A^+(E)}} - k_I^b\theta_{A^+(ads)}, \tag{6}$$

$$\frac{o_s}{N_s}q_{II} = k_{II}^f\theta_{A^+(ads)}\exp\left(\frac{\beta\Delta\Phi F}{RT}\right)$$
$$- k_{II}^b\theta_{B(ads)}\exp\left(-\frac{(1-\beta)\Delta\Phi F}{RT}\right), \tag{7}$$

$$\frac{o_s}{N_s}q_{III} = k_{III}^f\theta_{B(ads)} - k_{III}^b\theta_{C(ads)}, \tag{8}$$

and

$$\frac{o_s}{N_s}q_{IV} = k_{IV}^f\theta_V\frac{c_{C(E)}}{C^0_{C(E)}} - k_{IV}^b\theta_{C(ads)}, \tag{9}$$

with forward and backward reaction rate constants, k^f and k^b, symmetry factor, β, standard state concentrations, C^0, and temperature, T. Reaction II is an electrochemical reaction and thus includes an exponential dependency of electrical potential $\Delta\Phi$ at the interface. Surface fraction θ_B and reaction rate constants k_{II}^f, k_{II}^b, k_{III}^f and k_{III}^b are provided as input parameters from the kMC model as given in

the following sections. Surface fractions of vacant sites V(ads) are determined as

$$\theta_V = 1 - \theta_{A^+(ads)} - \theta_{B(ads)} - \theta_{C(ads)}. \tag{10}$$

Forward and backward rate constants of the sorption processes I and IV are independent of the kMC model and determined by the following equations:

$$k_I^f = k_I\exp\left(\frac{-E_I^A}{RT}\right), \tag{11}$$

$$k_I^b = k_I\exp\left(\frac{-(E_I^A - \Delta G_I^0)}{RT}\right), \tag{12}$$

$$k_{IV}^f = k_{IV}\exp\left(\frac{-E_{IV}^A}{RT}\right), \tag{13}$$

and

$$k_{IV}^b = k_{IV}\exp\left(\frac{-(E_{IV}^A - \Delta G_{IV}^0)}{RT}\right) \tag{14}$$

with activation energy of the forward process, E^A, and standard state Gibbs free energy of the forward process, ΔG^0.

2.3. Kinetic Monte Carlo model

The scope of the kMC model is illustrated in Fig. 1(C). The model includes the reaction processes II and III. Only species B is considered explicitly, i.e. sites covered with B. The species A^+ and C are assumed to be homogeneously distributed on the sites that are not covered by B, referred to as ¬B site. The fraction of surface species A^+(ads) on ¬B sites, $\theta_{A^+(ads),\neg B}$, surface species C(ads) on ¬B sites, $\theta_{C(ads),\neg B}$, and the electrical potential, $\Delta\Phi$, are provided as input parameters from the continuum model. Details about model interaction are provided in the next section.

Kinetic equations for reaction II and III are solved using a rejection-free kMC algorithm with variable step size. The kMC algorithm is based on examples provided by Burghaus (2006). Steps within the algorithm are explained in the following. In general the kMC algorithm includes the following actions with every kMC step i:

1. Calculate microscopic rate $\Gamma_i^{l,j}$ of considered microscopic processes $j \in \{1, 2, 3, 4\}$ on the lattice sites $l \in \{z|z \in \mathbb{N}, z \leq n^l\}$.
2. Calculate the step time length Δt_{i+1} applying a random number $\zeta_1 \in (0, 1)$.
3. Select one microscopic process $J_i \in \{1, 2, 3, 4\}$ and one lattice site $L_i \in \{z|z \in \mathbb{N}, z \leq n^l\}$ taking into account the microscopic rates $\Gamma_i^{l,j}$ applying a second random number $\zeta_2 \in (0, 1)$.
4. Perform the selected process J_i on surface site L_i.
5. If $i < \iota$, with ι being the last step of the kMC sequence, go to 1. The last step ι is defined using the time steps of the kMC sequence t_s^{seq}, which are set within the MPA (details are provided in the following section).

Thereby, the kMC model sets up a cubic lattice with $n^l = n_x^l \cdot n_y^l$ lattice sites, with lattice state $\vartheta_i^l \in \{0, 1\}$ at lattice site l. A lattice site covered by B yields $\vartheta_i^l = 1$, i.e. B site, and a lattice site not covered by B yields $\vartheta_i^l = 0$, i.e. ¬B site. Within the kMC algorithm, in every kMC step i lattice state is changed. The lattice site is selected according to microscopic rates of the considered microscopic processes. A lattice site transfers $\vartheta_i^l = 0$ to $\vartheta_i^l = 1$ with the microscopic rate

$$\Gamma_i^{l,1} = (1 - \vartheta_i^l)k_{II}\theta_{A^+(ads),\neg B}\exp\left(\frac{-E_{II}^A}{RT}\right)\exp\left(\frac{\beta\Delta\Phi F}{RT}\right) \tag{15}$$

corresponding to a microscopic forward step of process II and

$$\Gamma_i^{l,4} = (1 - \vartheta_i^l) k_{\text{III}} \theta_{\text{C(ads)},\neg\text{B}} \exp\left(\frac{-(E_{\text{III}}^A - \Delta G_{\text{III}}^0)}{RT}\right) \quad (16)$$

corresponding to a microscopic backward step of process III. Accordingly, a lattice site transfers from $\vartheta_i^l = 1$ to $\vartheta_i^l = 0$ with the microscopic rate

$$\Gamma_i^{l,2} = \vartheta_i^l k_{\text{II}} \exp\left(\frac{-(E_{\text{II}}^A - \Delta G_{\text{II}}^0)}{RT}\right) \exp\left(\frac{-(1-\beta)\Delta\Phi F}{RT}\right) \quad (17)$$

corresponding to microscopic backward step of process II and

$$\Gamma_i^{l,3} = \vartheta_i^l k_{\text{III}} \exp\left(\frac{-E_{\text{III}}^A}{RT}\right) \quad (18)$$

corresponding to a microscopic forward step of process III. With this, a total of $n^j = 4$ microscopic processes are considered in the kMC model. The microscopic rates include the following input values: $\Delta\Phi_s$, $\theta_{\text{A}^+\text{(ads)},\neg\text{B}}$ and $\theta_{\text{C(ads)},\neg\text{B}}$, which are constant within a kMC sequence. Updating those input values with every kMC time step i is computationally very expensive and thus not feasible. Assuming constant values causes an error in the coupled simulation, which is evaluated and discussed to assess the coupling quality as detailed below.

In every kMC step i, first the step time length is calculated based on a uniform distribution random number $\zeta_1 \in (0, 1)$ as

$$\Delta t_{i+1}^{\text{kMC}} = \frac{-\ln(\zeta_1)}{\Gamma_i^{\text{tot}}}, \quad (19)$$

with Γ_i^{tot} being the total microscopic rate, which is calculated as

$$\Gamma_i^{\text{tot}} = \sum_{l=1}^{n^l} \sum_{j=1}^{n^j} \Gamma_i^{l,j}. \quad (20)$$

The discrete time at the following kMC time step $i+1$ can be calculated with

$$t_{i+1}^{\text{kMC}} = t_i^{\text{kMC}} + \Delta t_{i+1}^{\text{kMC}}. \quad (21)$$

Further, in every kMC step, one of the n^j microscopic processes j and one of the n^l lattice sites l, is selected, with respect to the microscopic rate $\Gamma_i^{l,j}$ as given in Eqs. (15)–(18), applying a second uniform distribution random number $\zeta_2 \in (0, 1)$ according to

$$\frac{\sum_{l=1}^{L_i} \sum_{j=1}^{J_i-1} \Gamma_i^{l,j}}{\Gamma_i^{\text{tot}}} < \zeta_2 \leq \frac{\sum_{l=1}^{L_i} \sum_{j=1}^{J_i} \Gamma_i^{l,j}}{\Gamma_i^{\text{tot}}} \quad (22)$$

with J_i being the selected process and L_i being the selected grid point. A boolean Ψ, which indicates the selection of a process j within a kMC step i is determined as

$$\Psi_i^j = \begin{cases} 1, & \text{if } J_i = j \\ 0, & \text{otherwise} \end{cases} \quad (23)$$

to enable counting how often a certain process j occurs.

2.4. Sequence and model interaction

As shown in the previous sections, both models rely on input of the respective other model. This requires to pass input parameters between the models, which needs to be handled by the MPA. One possibility is to split the simulation in time sequences. In each time sequence both models are simulated one after another with fixed sequence specific input parameters. Input of the model simulated first needs to be estimated, while the input of the second model can be evaluated using the results of the first model.

The simulation procedure during a sequence is illustrated in Fig. 3. It can be seen that within a sequence s the continuum and
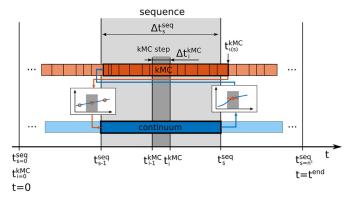

Fig. 3. Processes during one sequence in the coupled simulation.

the kMC model are solved. The sequence period is determined as

$$\Delta t_s^{\text{seq}} = \frac{t^{\text{end}}}{n^{\text{seq}}} \quad (24)$$

where t^{end} is the simulation time and n^{seq} the number of sequences. This determines the end time of the following sequence $s+1$

$$t_{s+1}^{\text{seq}} = t_s^{\text{seq}} + \Delta t_{s+1}^{\text{seq}} \quad (25)$$

The mean-time corresponding to a sequence is defined as

$$\bar{t}_s^{\text{seq}} = \frac{t_s^{\text{seq}} + t_{s-1}^{\text{seq}}}{2} \quad (26)$$

The time of the last kMC step i corresponding to a sequence s, ι, is not equal to but slightly higher than the end time of the sequence t_s^{seq}, as kMC step time length is determined using a random number. The last kMC step ι can be determined as a function of s, i.e. $\iota = f(s)$, according to

$$\iota = \max(i) \in \{i | t_{s-1}^{\text{seq}} < t_{i-1}^{\text{kMC}} \leq t_s^{\text{seq}}\} \quad (27)$$

Further, the sequence ς, corresponding to of a certain point in time can be determined as a function of i, i.e. $\varsigma = f(i)$, according to

$$t_{\varsigma-1}^{\text{seq}} < t_{i-1}^{\text{kMC}} \leq t_\varsigma^{\text{seq}} \quad (28)$$

The input parameters for the kMC model in step i are evaluated with the continuum model at the mean time $\bar{t}_\varsigma^{\text{seq}}$ of the sequence ς as

$$\theta_{\text{A}^+\text{(ads)},\neg\text{B}}(i) = \frac{\theta_{\text{A}^+\text{(ads)}}(\bar{t}_\varsigma^{\text{seq}})}{1 - \theta_{\text{B(ads)}}(\bar{t}_\varsigma^{\text{seq}})} \quad (29)$$

$$\theta_{\text{C(ads)},\neg\text{B},s}(i) = \frac{\theta_{\text{C(ads)}}(\bar{t}_\varsigma^{\text{seq}})}{1 - \theta_{\text{B(ads)}}(\bar{t}_\varsigma^{\text{seq}})} \quad (30)$$

$$\Delta\Phi(i) = \Delta\Phi(\bar{t}_\varsigma^{\text{seq}}) \quad (31)$$

which are functions of kMC time step i and constant within a sequence.

The input to the continuum model needs to be provided as a continuous function of time t. In the following, the required evaluation of kMC simulations to determine these inputs is shown. The kMC simulations are performed as parallel instances v, i.e. several kMC simulations with equal simulation input are performed in parallel during each sequence. This allows one to statistically evaluate the kMC output as shown below. The mean surface fraction of species B within one simulation instance v and one sequence s is determined as

$$\hat{\theta}_{\text{B}}(s) = \frac{\sum_{i=\iota(s-1)}^{\iota(s)} \left(\Delta t_i^{\text{kMC}} \sum_{l=1}^{n^l} \vartheta_i^l\right)}{\sum_{i=\iota(s-1)}^{\iota(s)} \left(\Delta t_i^{\text{kMC}} n^l\right)} \quad (32)$$

With this the mean surface fraction of ¬B sites can be calculated as

$$\hat{\theta}_{\neg B}(s) = 1 - \hat{\theta}_B(s) \tag{33}$$

Using the average ¬B site fraction, the effective average fraction of the other species can be determined, as given in the following for the example of the A^+ species:

$$\hat{\theta}_{A^+} = \theta_{A^+(ads),\neg B} \cdot \hat{\theta}_{\neg B} \tag{34}$$

This can be used to determine the effective reaction rate constants for forward and backward rates of process II and III, as shown in the following at the example of forward reaction of process II:

$$\hat{k}_{II}^f(s) = \frac{\sum_{i=\iota(s-1)}^{\iota(s)} \Psi_i^1}{\Delta t_s^{seq} n^l \Delta L^2}$$
$$\cdot \frac{1}{N_s \hat{\theta}_{A^+(ads)} \exp\left(\frac{\beta \Delta \Phi F}{RT}\right)}. \tag{35}$$

We note, that indeed, instead of reaction rate constants, one could also directly pass the reaction fluxes, e.g. q_{II}, from the kMC to the continuum model. However, for numerical stability of the solution it is advantageous to include some general dependencies within the continuum solution, if possible. For instance, here, we include the general dependency of the forward reaction of process II on surface fraction $\theta_{A^+(ads)}$ within the continuum model, i.e. as given by Eq. (7). Synchronization of the fluxes between kMC and continuum model is realized by adapting the rate constants k_{II}^f and k_{II}^b in the continuum model. Passing rate constants instead of fluxes, prevents, for instance, negative values of $\theta_{A^+(ads)}$ in the continuum simulation and thus improves numerical stability, as stated above.

As mentioned above, kMC simulations are performed in parallel instances v. Thus, an output parameter $\hat{p}_{s,v}$, e.g. $\hat{\theta}_{B,s,v}$, depends on s and v. The mean value of the n^{par} parallel instances can thus be calculated as

$$M_s^p = \frac{\sum_{v=1}^{n^{par}} \hat{p}_{s,v}}{n^{par}}, \tag{36}$$

while the standard deviation of the calculated value M_s^p can be approximated as

$$S_s^p \approx \sqrt{\frac{1}{n^{par}(n^{par}-1)} \sum_{v=1}^{n^{par}} |\hat{p}_{s,v} - M_s^p|^2} \tag{37}$$

It is noted that S_s^p, indeed, is only an approximation of the standard deviation, which is achieved by evaluating a sample of kMC simulations of the size n^{par}. In order to determine $p(t)$, e.g. $\theta_B(t)$, for the continuum model a cubic smoothing spline is determined, that minimizes

$$\kappa \sum_{s=1}^{n^{seq}} |M_s^p - p(\bar{t}_s^{seq})| + (1-\kappa) \int \left| \frac{d^2 p(t)}{dt^2} \right|^2 dt \tag{38}$$

with smoothing factor κ. This yields the continuum input parameters as continuous functions of time t: $k_{II}^f(t)$, $k_{II}^b(t)$, $k_{III}^f(t)$, $k_{III}^b(t)$, and $\theta_B(t)$.

2.5. Direct coupling algorithms

The previous section showed the continuum model, the kMC model, the sequencing and the exchanged values in detail. However, the order of passing values and the interpretation of simulation outputs have not yet been discussed. There are various options to realize this coupling which differ significantly in stability, accuracy and computation time. Here, a systematic analysis and comparison allows to show the pros and cons of the approaches, and

thus educated selection and tailoring in future studies. Three different algorithms for coupling of both models are presented in this section.

In every algorithm within a sequence s, the kMC and the continuum model is solved. However, the order and the interpretation of the outputs can vary between algorithms. The first, MPA1, is shown in Fig. 4(a). Here, within a sequence, the continuum model is simulated first. In the second, MPA2, the order is switched, as can be seen in Fig. 4(b). The third, MPA3, as shown in Fig. 4(c), has the same sequential order as MPA1, but includes an estimation loop, which repeats one sequence s until the results are within a defined tolerance. As will be shown, the additional loop considerably increases computational cost of the overall simulation. The algorithms include a filtering step of the kMC data to account for the stochastic nature of kMC, and a prediction step to predict the output of the second model in the upcoming sequence. This prediction step can cause an error in the overall simulation, which will be referred to as the *prediction error*. For MPA3, an estimation step is also introduced, in which the output of the kMC step is estimated based on the previous iterations. The intention is to correct the initially introduced prediction error. The simulation is terminated as soon as a specified end criteria is reached, which can be, for instance, $t > t^{end}$ with t^{end} being the specified end time.

In MPA1 and MPA3, the output of the kMC model for the upcoming sequence is predicted as

$$M_{s+1}^p = M_s^p + \frac{(M_s^p - M_{s-1}^p)}{(\bar{t}_s^{seq} - \bar{t}_{s-1}^{seq})} (\bar{t}_{s+1}^{seq} - \bar{t}_s^{seq}) \tag{39}$$

in the upcoming sequence $p(t)$ is calculated based on Eq. (38) including this prediction. In MPA2 the output of the continuum model is predicted as

$$p(\bar{t}_{s+1}^{seq}) = p(t_s^{seq}) + \frac{dp(t_s^{seq})}{dt} \frac{\Delta t_{s+1}^{seq}}{2}. \tag{40}$$

Filtering of the kMC output is realized using the smoothing factor κ as given in Eq. (38), while a smoothing factor of 1 yields no smoothing and smoothing factor of 0 yields an approximation by a linear function. The filtering in MPA1 includes the predicted kMC output based on Eq. (39). In the first sequence, $s = 0$, the input of the first model is estimated using the start values at $t = 0$, which are provided in Table 2.

MPA3 includes an additional estimation loop, which is used to correct errors caused by the prediction step. The estimation procedure is provided in detail in the following. M_e^{p*} is the mean output of value p in estimation step e and E_e^M is the estimation of the mean output. The estimation of the upcoming step $e + 1$ is calculated as

$$E_{e+1}^M = E_e^M + K_P(M_e^{p*} - E_e^M) + K_I \sum_{z=1}^{e} (M_z^{p*} - E_z^M) \tag{41}$$

while the estimate of the standard deviation E_e^S is calculated accordingly, as

$$E_{e+1}^S = E_e^S + K_P(S_e^{p*} - E_e^S) + K_I \sum_{z=1}^{e} (S_z^{p*} - E_z^S) \tag{42}$$

Equations likewise consider the difference between the estimated value, e.g. E_e^M, and the actual output mean value, e.g. M_e^{p*}, in the previous step as well as the sum up to the last iteration step, which are thereby weighted by a proportional K_P and an integral factor K_I, respectively. This algorithm resembles the setup of a proportional-integral (PI) controller. Due to the fluctuations of the kMC output, E_e^M and M_e^{p*} are unlikely to converge to exactly the same value. An acceptable tolerance between both values needs to be defined, which in this work is

$$E_e^M - E_e^S \lambda < M_e^{p*} < E_e^M + E_e^S \lambda \tag{43}$$

Fig. 4. Illustration of the multiparadigm algorithms MPA1 (a), MPA2 (b) and MPA3 (c).

with λ being the tolerance factor to scale the tolerance relative to the standard deviation, i.e. fluctuations of the output. As soon as Eq. (43) is true for all M_e^{p*}, the output of the sequence is defined as

$$M_s^p = M_e^{p*} \tag{44}$$

and the next sequence is calculated.

2.6. Error estimation

To estimate the error of the coupled simulation, results are compared to a pure continuum solution. This is possible because no heterogeneity is included in this kMC model. Nevertheless, the approach enables to consider heterogeneity in a coupled simulation as we showed in our previous work on chemical and electrochemical degradation in Lithium-ion batteries (Röder et al., 2017).

The kMC model covers the calculation of the reaction rate constants of reaction II and III, which for the homogeneous case can be determined as

$$k_{II}^f = k_{II} \exp\left(\frac{-E_{II}^A}{RT}\right), \tag{45}$$

$$k_{II}^b = k_{II} \exp\left(\frac{-(E_{II}^A - \Delta G_{II}^0)}{RT}\right), \tag{46}$$

$$k_{III}^f = k_{III} \exp\left(\frac{-E_{III}^A}{RT}\right), \tag{47}$$

and

$$k_{III}^b = k_{III} \exp\left(\frac{-(E_{III}^A - \Delta G_{III}^0)}{RT}\right). \tag{48}$$

Table 2
Model parameters.

Parameter	Value
Ideal gas constant R [J mol^{-1} K^{-1}]	8.314
Temperature T [K]	300
Faraday constant [A s mol^{-1}]	96,485.33289
Specific surface area a_s [m^{-1}]	1×10^6
Double layer capacitance C^{DL} [F m^{-2}]	0.2
Distance between lattice sites ΔL [m]	6×10^{-10}
Site density N_s [m^{-2}]	$1/\Delta L^2$
Site-occupancy number o_s [mol^{-1}]	6.022×10^{23}
Input amplitude $\bar{A}$ [A m^{-2}]	1
Input frequency f [s^{-1}]	0.1
Symmetry factor β [–]	0.5
Rate constant k_I [s^{-1}]	1×10^{13}
Rate constant k_{II} [s^{-1}]	1×10^{10}
Rate constant k_{III} [s^{-1}]	1×10^{10}
Rate constant k_{IV} [s^{-1}]	1×10^{13}
Activation energy E_I^A [kJ mol^{-1}]	45
Activation energy E_{II}^A [kJ mol^{-1}]	50
Activation energy E_{III}^A [kJ mol^{-1}]	50
Activation energy E_{IV}^A [kJ mol^{-1}]	45
Standard state Gibbs free energy ΔG_I^0 [kJ mol^{-1}]	0
Standard state Gibbs free energy ΔG_{II}^0 [kJ mol^{-1}]	−0.965
Standard state Gibbs free energy ΔG_{III}^0 [kJ mol^{-1}]	−0.965
Standard state Gibbs free energy ΔG_{IV}^0 [kJ mol^{-1}]	1.93
Standard state concentration of species A$^+$(E) $C_{A^+(E)}^0$ [mol m^{-3}]	1000
Standard state concentration of species C(E) $C_{C(E)}^0$ [mol m^{-3}]	1000
Initial potential $\Delta\Phi(t=0)$ [V]	0
Initial concentration of species $c_{A^+(E)}(t=0)$ [mol m^{-3}]	1000
Initial concentration of species $c_{C(E)}(t=0)$ [mol m^{-3}]	1000
Initial surface fraction of species $\theta_{A^+(ads)}(t=0)$ [–]	0.18
Initial surface fraction of species $\theta_{B(ads)}(t=0)$ [–]	0.26
Initial surface fraction of species $\theta_{C(ads)}(t=0)$ [–]	0.38

Further, the model covers the balancing of species B on the adsorption site. In the purely continuum model this balance is included as

$$\frac{N_s}{o_s} \frac{d\theta_B(ads)}{dt} = q_{II} - q_{III} \tag{49}$$

By supplementing the continuum model as provided in Section 2.1 with Eqs. (45)–(49), an accurate reference solution can be determined. In summary, this yields the following possible solutions for the simulation of the example problem:

- MPA1: Continuum model of Section 2.1 coupled with kMC model of Section 2.2 using MPA1 algorithm.
- MPA2: Continuum model of Section 2.1 coupled with kMC model of Section 2.2 using MPA2 algorithm.
- MPA3: Continuum model of Section 2.1 coupled with kMC model of Section 2.2 using MPA3 algorithm.
- Reference: Continuum model of Section 2.1 supplemented by Eqs. (45)–(49).

To determine errors of the MPA algorithms, results are compared to the reference solution. Thus, absolute errors of the MPA solutions can be determined, which is shown for the example of the surface fraction of species B calculated by MPAx with $x \in \{1, 2, 3\}$ in the following:

$$\theta_B^{error}(\bar{t}_s^{seq}) = \theta_B^{MPAx}(\bar{t}_s^{seq}) - \theta_B^{reference}(\bar{t}_s^{seq}). \tag{50}$$

Further, the absolute average error of potential, reaction rate constants, and surface fraction over all sequences are determined as

$$\bar{\Delta\Phi}^{error} = \frac{\sum_{s=1}^{n^{seq}} |\Delta\Phi^{error}(\bar{t}_s^{seq})|}{n^{seq}}, \tag{51}$$

$$\bar{k}^{error} = \frac{\sum_{s=1}^{n^s} |k_{II}^{f,error}(\bar{t}_s^{seq})|}{4 \cdot n^{seq}} + \frac{\sum_{s=1}^{n^{seq}} |k_{II}^{b,error}(\bar{t}_s^{seq})|}{4 \cdot n^{seq}}$$
$$+ \frac{\sum_{s=1}^{n^{seq}} |k_{III}^{f,error}(\bar{t}_s^{seq})|}{4 \cdot n^{seq}} + \frac{\sum_{s=1}^{n^{seq}} |k_{III}^{b,error}(\bar{t}_s^{seq})|}{4 \cdot n^{seq}}, \tag{52}$$

and

$$\bar{\theta}^{error} = \frac{\sum_{s=1}^{n^{seq}} |\theta_{A^+}^{error}(\bar{t}_s^{seq})|}{4 \cdot n^{seq}} + \frac{\sum_{s=1}^{n^{seq}} |\theta_B^{error}(\bar{t}_s^{seq})|}{4 \cdot n^{seq}}$$
$$+ \frac{\sum_{s=1}^{n^{seq}} |\theta_C^{error}(\bar{t}_s^{seq})|}{4 \cdot n^{seq}} + \frac{\sum_{s=1}^{n^{seq}} |\theta_V^{error}(\bar{t}_s^{seq})|}{4 \cdot n^{seq}}, \tag{53}$$

respectively. Absolute errors for reaction constants for forward and backward reaction and those of the surface fractions are averaged; this allows to reduce the number of variables and thus enables a focused discussion and comparison of the MPAs.

The errors, as introduced above, are used to evaluate the overall error of the coupled simulation. However, those evaluations barely allow to assign errors to certain causes. Most relevant causes are the fluctuation of the kMC (fluctuation error), the quasi steady state assumption within a kMC sequence neglecting the transient change of the input parameter (transition error), and the prediction of the input values (prediction error). To decompose the effect of those contributions, they are investigated separately, as will be outlined in the following. By assuming constant values for the input of the kMC model, as given in Eqs. (29)–(31), an error is introduced, which will be referred to as transition error. The error can be decomposed by using the according assumption in the reference solution. In the following, this is shown for the example of the electrical potential $\Delta\Phi$, as used in Eq. (7):

$$\Delta\Phi(t) = \Delta\Phi(\bar{t}_s^{seq}) \tag{54}$$

for $t_{s-1}^{seq} < t \leq t_s^{seq}$. According to Eq. (40) the error of MPA2, which includes the prediction, can be introduced at the example of $\Delta\Phi$ by assuming

$$\Delta\Phi(t) = \Delta\Phi(t_{s-1}^{seq}) + \frac{d\Delta\Phi(t_{s-1}^{seq})}{dt} \frac{\Delta t_s^{seq}}{2} \tag{55}$$

According to Eq. (39) the error of MPA1, which includes the prediction, can be introduced at the example of θ_B by identification of

$$M_s^{\theta_B} = M_{s-1}^{\theta_B} + \frac{(M_{s-1}^{\theta_B} - M_s^{\theta_B})}{(\bar{t}_{s-1}^{seq} - \bar{t}_s^{seq})} (\bar{t}_s^{seq} - \bar{t}_{s-1}^{seq}) \tag{56}$$

for $t_{s-1}^{seq} < t \leq t_s^{seq}$ and application of the smoothing function in Eq. (38) to determine $\theta_B(t)$. The assumptions that are given in Eqs. (55) and (56), however, also include a transition error, which need to be subtracted to decompose the error of the prediction. The errors caused by the fluctuation of the kMC output can be quantified by the standard deviation of the kMC output, i.e. Eq. (37). To sum up, the particular error contributions in this work have been estimated as absolute errors, which are calculated as difference between the reference model and the reference model with modifications outlined above. With this, the contributions to the overall error of the three causes listed above, can be decomposed for any value, e.g. the surface fraction of B θ_B, as given in the following:

- transition error of value = value in reference model modified by assumptions according to Eq. (54) - value in reference model;
- prediction error of value (MPA1) = value in reference model modified by assumptions according to Eq. (55) - transition error - value in reference model;
- prediction error of value (MPA2) = value in reference model modified by assumptions according to Eq. (56) - transition error - value in reference model;
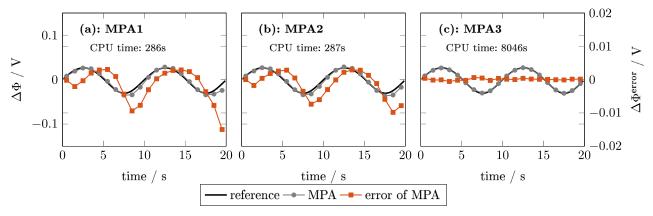- fluctuation error = S_s^p in Eq. (37).

Fig. 5. Difference in the electrical potential $\Delta\Phi$ and absolute error compared to the continuum solution, and the CPU time for algorithms MPA1, MPA2, and MPA3.

2.7. Simulation scenario and parameters

The input into the simulation triggering the reaction is an externally applied current I. The current leads also to charge and discharge of the electrochemical double layer and change of the electrical potential $\Delta\Phi$ at the electrochemical surface. Since the presented approach is designed to be applied to investigate dynamic operation of electrochemical systems, also a dynamic signal is applied. We define the sinusoidal input current as

$$I = \bar{A}\sin(2\pi ft) \tag{57}$$

with amplitude $\bar{A}$ and the frequency f. All parameters are listed in Table 2. Parameters are chosen in a physically reasonable order of magnitude but mainly to provide illustrative simulation results. All models are implemented and solved in MATLAB. Ordinary differential equations are solved by the ode15s solver. Simulations are performed in Matlab on a 64-bit linux system with Intel Core$^{\text{TM}}$ i7-3770 CPU with 3.40 GHz $\times 8$ and 15.5GB RAM.

3. Results and discussion

To show the impact of the type of coupling algorithm and configuration, simulations were performed with a varying number of lattice sites n^l, number of sequences n^{seq}, proportional factor K_P, tolerance factor λ, and smoothing factor κ. Multiparadigm simulations are benchmarked by comparison to a pure continuum solution, indicated as reference. The standard configuration of the algorithms is defined by $n^l = 10^2$, $n^{\text{par}} = 16$, $K_P = 0.2$, $\lambda = 1$, and $\kappa = 1$ and is always applied if not stated otherwise.

3.1. Numerical accuracy of the coupling algorithms

Fig. 5 shows the electrical potential $\Delta\Phi$ for the continuum model and for the multiparadigm algorithms MPA1, MPA2, and MPA3 using the reference configuration. Due to the sinusoidal signal input of the external current I, the electrical potential increases and decreases as a sinusoid also. All three algorithms are in good agreement with the continuum solution with deviations below 5% relative to the voltage amplitude. The errors of MPA1 and MPA2 are significantly higher than MPA3. Further, MPA1 and MPA2 both possess an oscillatory increase and decrease of the error. The peaks of the errors are increasing for both algorithms towards the end of the simulation and are comparable regarding positions in time and magnitude, which suggests both errors are of the same origin. In contrast, the error of MPA3 neither increases nor shows a comparable systematic behavior. The electrical potential is determined by the continuum part of the MPAs with Eq. (1), and depends on the current input I and the rate of reaction II, q_{II}. Since the input I is
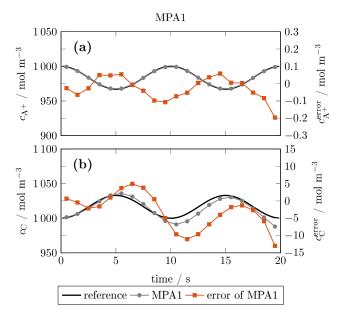

Fig. 6. Concentration and absolute error of species (a) A$^+$ and (b) C for MPA1.

equivalent for all simulations, the error of the electrical potential originates from an error of the reaction rate q_{II}. In the MPA simulations, this rate directly depends on three kMC outputs, being the forward and backward reaction rate constants, k_{II}^f and k_{II}^b, and the surface fraction of species B, θ_{B}. Although the simulation accuracy is considerably higher for MPA3 compared to MPA1 and MPA2, its computational cost is nearly 30 times higher, as given in Fig. 5.

While the errors for MPA1 and MPA2 have the same systematic behavior, MPA1 had a larger maximum error and so was analyzed in more detail. In Fig. 6, the concentrations of species A$^+$ and C in solution are compared for the continuum-only model and MPA1. Just as for the electrical potential, the concentrations are solved within the continuum part of the MPAs, and errors indirectly originate from errors in the kMC output. The concentration of species A$^+$ is in very good agreement with the continuum solution, whereas the concentration of species C has a considerable deviation, as the absolute error of the concentration is about two orders of magnitude higher compared to the absolute error of concentration of species A$^+$. Both errors show the same systematic behavior as previously seen for the electrical potential. The concentrations are influenced by surface fractions of species A$^+$, C, and vacancies V, so the surface fractions and their errors are discussed next.
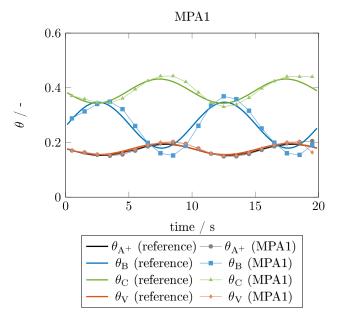
Fig. 7. Surface fraction of species A^+, B, C, and vacancies V for the continuum solution and MPA1.
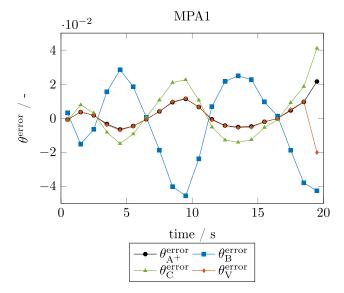

Fig. 8. Absolute error of surface fraction of species A^+, B, C, and vacancies V for MPA1.

In Fig. 7, MPA1 is further evaluated for the surface fractions θ_i of species A^+, B, C, and vacancies V. Again, the impact of the sinusoidal input can be seen, as the surface fractions decrease and increase sinusoidally as well. The amplitude of the oscillations is lowest for species A^+ and V and highest for species B. The mean and amplitude of the surface fraction of vacant sites and of species A^+ are very similar. The deviations of the surface fractions in MPA1 are highest for species B and lowest for species A^+ and vacancies V, which is shown in detail in Fig. 8. The errors in the surface fractions originate from errors in the kMC outputs and in particular directly from error in the surface fraction θ_B. Since surface fractions of all species sum up to 1 as given by Eq. (10), the absolute error in the surface fractions sum up to 0. As such, an error in the surface fraction of species B forces a distribution of this error on the other surface fractions. The share of this error is almost equal for species A^+ and vacancies V. The very low observed error in the concentration of A^+ in the solution can be explained. Comparing

to the continuum solution, the surface fractions of the vacancies V and of species A^+ impact the forward and backward rate of process I, respectively. Since both surface fractions have almost the same values and errors, the impacts compensate each other leading to a very low error propagation to the concentration of A^+ in the solution. In contrast, for reaction 4, the values and errors of the surface fraction of C considerably differ leading to a distinct and significant error propagation to the solution concentration C. The results illustrate that the propagation of an error in a multiscale algorithm can depend considerably on the system and its parameters.
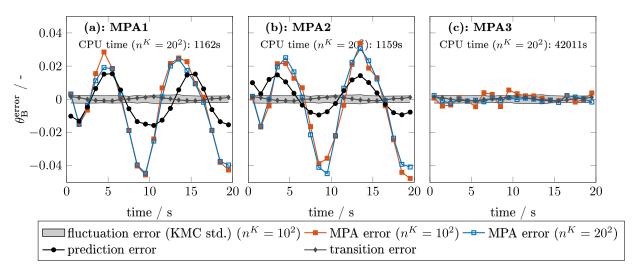
The magnitude and systematic nature of the errors of MPA1 and MPA2 (not shown here in detail) were found to be comparable, and the order of the sequence was of minor relevance for the simulation accuracy and computational cost. MPA3 significantly improved the accuracy but with much higher computational cost. The systematic oscillatory nature of the errors in MPA1 and MPA2, which do not appear in MPA3, suggests a different origin. The next section analyzes the errors in detail and discusses efficient tuning of the algorithms to reduce the overall simulation error.
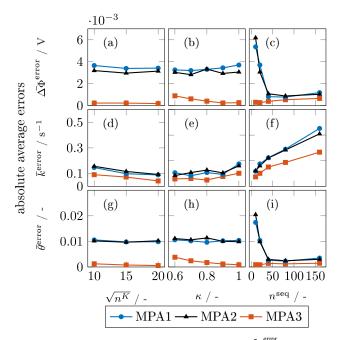
3.2. Algorithm tuning

By examining the system states (i.e. potentials, concentrations, and surface fractions), the impact of MPAs on the simulation error has been shown. Errors can originate thereby from the coupling of the continuum and kMC models, as well as the stochastic nature of the kMC model. Different algorithms can lead to very different systematic errors and magnitudes of the errors. In particular, a considerable difference between algorithms without estimation correction, i.e. MPA1 and MPA2, and an algorithm including an estimation correction, i.e. MPA3, could be seen. As introduced above, we distinguish three types of errors: (i) prediction error, (ii) transition error, and (iii) fluctuation error. The errors of the reaction rate constants were not dependent on time and so do not include any prediction or transition errors. As such, only the results for the surface fraction θ_B are discussed in detail.

The various absolute errors of θ_B for the MPAs are shown in Fig. 9. The prediction and transition errors are oscillatory. The fluctuation error induced by the kMC simulation is nearly constant during the whole simulation. The prediction error is considerably larger than the transition and fluctuation errors, which are of the same order of magnitude. The overall error for MPA1 is oscillatory and strongly correlates with the prediction error, especially during the first quarter of the simulation; as the simulation proceeds, the overall error of the MPA1 increases and exceeds the prediction error. The errors accumulate and the MPA solution becomes somewhat out of phase with ongoing simulation time. A similar correlation between the prediction error and overall error occurs for MPA2. The prediction error of MPA2 is slightly lower, with some increase in peak overall error with time. For MPA3, the initial prediction is equal to that for MPA1, but is corrected by the estimation correction loop and so is not seen in the Fig. 9(c). The estimation correction leads to a considerable decrease of the overall error. The prediction error is the result of the linear interpolation using Eqs. (39) and (40). We note that the prediction error may be reduced by using higher order extrapolations instead. However, this could also increase the error or cause numerical instabilities. Detailed investigations of these effects are out of the scope of this article, but nevertheless should be addressed in future work.

The fluctuation error can be reduced by increasing the number of lattice sites, such as increasing the grid size. Fig. 9 indicates that increasing n^l from 10^2 to 20^2 did not reduce the overall error of MPA1 and MPA2, which is dominated by the prediction error, but did reduce the overall error for MPA3. The reduction in fluctuation error for MPA3 results in its overall error becoming more correlated to the transition error. These results illustrate that increasing

Fig. 9. Errors for (a) MPA1, (b) MPA2, and (c) MPA3 for surface fraction of species B for $n^l = 10^2$ and $n^l = 20^2$, as well as prediction, transition, and fluctuation errors for $n^l = 10^2$. The CPU time for $n^l = 20^2$ is given in each subplot.

Fig. 10. Absolute average errors for the electrical potential $\bar{\Delta\Phi}^{\text{error}}$, reaction rates $\bar{k}^{\text{error}}$, and surface fractions $\bar{\theta}^{\text{error}}$ for varying field size, smoothing factor, and number of sequences.

the number of lattice sites can only be an efficient strategy if the fluctuation error is the dominant, because of the overall simulation error.

The computational cost for the simulations with an increased field size are also provided in Fig. 9. The computational cost is significantly increased for all simulations compared to that of $n^l = 10^2$, given in Fig. 5. Again, the computational cost of MPA3 is significantly higher, i.e. more than 30 times higher, compared to MPA1 and MPA2. As such, there is a strong incentive to avoid a computationally expensive estimation-correction loop or to significantly reduce its iterations.
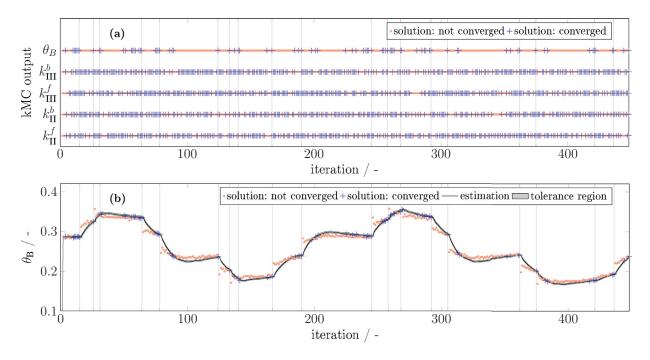
A systematic analysis of several measures to tune the MPA is shown by varying the field size n^l in Fig. 10(a), (d) and (g), the smoothing factor κ in Fig. 10(b), (e) and (h), and the number of sequences n^{seq} in Fig. 10(c), (f) and (i). The results show the effect of aforementioned measures on the averaged absolute errors of the electrical potential $\Delta\Phi$ in Fig. 10(a–c), the reaction rate constants

k_{II}^f, k_{II}^b, k_{III}^f and k_{III}^b in Fig. 10(d–f), and the surface fractions θ_{A^+}, θ_{B}, θ_{C}, and θ_{V} in Fig. 10(g), (h) and (i) for the three MPAs. The electrical potential can be interpreted as being an overall simulation error, as it represents the typical electrochemical model output. The reaction rates are kMC output variables that are independent of time and thus are only affected by fluctuation errors. The surface fractions are variables that are additionally directly affected by transition and prediction errors.

In Fig. 10(g), the errors in surface fractions are shown for a varying field size. The error is not affected by n^l for MPA1 and MPA2 since their errors are dominated by prediction error, but the error can be reduced for MPA3, which has no prediction error. Prediction errors are not affected by the number of lattice sites, which here makes increasing the field size a futile measure. In contrast, errors in the reaction rate constants, as shown in Fig. 10(d), are reduced for increasing the field size for all three algorithms. This error is only affected by fluctuation errors, which can be efficiently reduced by increasing the number of lattice sites. In Fig. 10(a), errors in the electrical potential is shown. Again, errors do not possess a clear dependency on field size for MPA1 and MPA2. In contrast, the errors of MPA3 can be slightly decreased with increased n^l. The error in the electrical potential is more strongly influenced by the error of the surface fraction than by the error of the reaction rate constant. For the variation in field size in Fig. 10, the error in MPA3 is an order of magnitude lower for electrical potential and surface fraction than for MPA1 and MPA2, but only about 40% lower for the reaction rate constant. The accuracy can be improved most by an estimation correction if the error is dominated by prediction error.

Next, consider the effects of smoothing the kMC output. Smoothing the kMC output, i.e. decreasing κ, reduced the overall error dominated by fluctuations of the kMC model (Fig. 10(e)). In contrast, smoothing had minimal effects on the overall error dominated by prediction error, i.e. the error in surface fraction θ for MPA1 and MPA2 (Fig. 10(h)), and increased smoothing increased the overall error for MPA3, which has no prediction error. The trends in the errors in the electrical potential are similar to those for θ (Fig. 10(b)), as those errors are more closely related than the errors in reaction rate constants in this simulation scenario.

Finally, consider the impact of varying the number of sequences, n^{seq}. An increasing number of sequences corresponds to a reduction of the time length of each sequence. Shorter time steps will reduce prediction length and improve accuracy of mean approximations within a kMC simulation, which will reduce the pre-

Fig. 11. (a) Convergence status during the iteration process and (b) estimated value, tolerance region, and actual kMC output for the surface coverage of B, θ_B. The convergence status of the kMC outputs are indicated as converged (blue plus), i.e. output is within the tolerance region, and not converged (red circle), i.e. output is outside the tolerance region. End time of a sequence is indicated by vertical gray lines with the last time step corresponding to t^{end}. This reference configuration has $n^l = 10^2$, $n_{\text{instance}} = 16$, $K_P = 0.2$, $\lambda = 1$, and $\kappa = 1$.

diction and transition errors. However, shorter time sequences will provide less data from the kMC model and thus result in an increase in the fluctuation error. The consequences can be observed in Fig. 10(c), (f) and (i). The errors in surface fraction θ for MPA1 and MPA2 in Fig. 10(i), which are dominated by the prediction error, can be significantly reduced to nearly the same magnitude as the error of MPA3 with an increasing number of sequences, n^{seq}, from 10 to 50. Further increase in the number of sequences increases the error.

In contrast, the error in the reaction rate constants for all MPAs increase with increasing number of sequences (Fig. 10(f)), as this error is dominated by kMC fluctuations, whose effects are increased by lowering the number of kMC steps. The trends in the errors for the electrical potential in Fig. 10(c) mostly mirror the errors for the surface fraction θ, except for stronger error reduction for MPA3 when decreasing the number of sequences, due to reduced fluctuation errors.

In general, the trend and magnitude of the errors for MPA1 and MPA2 are comparable for variations, and confirm that the sequential order of the stochastic and continuum models was of minor relevance. Distinct effects could be observed between algorithms with and without estimation correction and in particular for the number of sequences and smoothing of the kMC output. In general, the accuracy of MPA3 was the highest for all simulations and configurations shown here. The high accuracy was achieved by correcting the prediction error but with significantly increased computational cost. In summary, these results clearly examined the origin of the errors of the MPAs for the simulation scenario. The overall error was dominated by the largest of the three types of error (prediction, transition, fluctuation), and a reduction of less dominant errors did not reduce the overall error of the simulation.
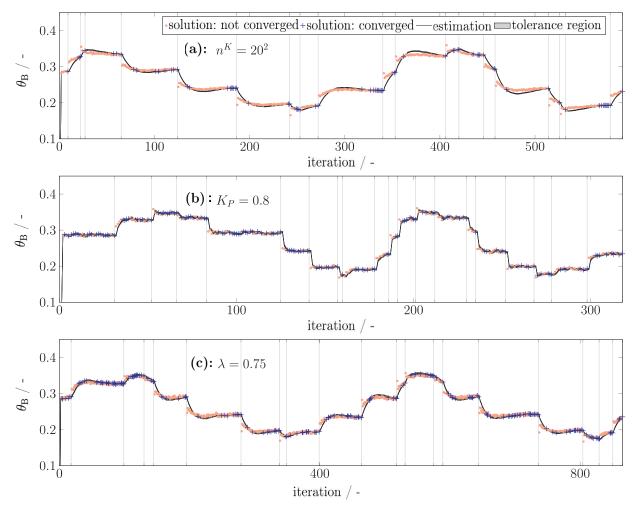
3.3. Efficient estimation correction

The estimation-correction loop in MPA3 evaluates the kMC output and iterates until the kMC output is within a defined tolerance region. The definition of the tolerance and the approach to control the solution into this tolerance region determines the accuracy and computational cost of MPA3. The computational cost is strongly related to the number of iterations needed in each time interval. To enable cost-effective multiscale simulations, therefore, it is important to identify a configuration of the algorithm that minimizes the number of iterations. This section analyzes the impact of n^l, K_P, and λ.

Fig. 11 shows convergence results for the reference configuration, which takes about 450 iterations to reach $t^{\text{end}} = 20$ s. The reaction rate constants are within tolerance for most of the iterations, because the parameters are independent of time and the estimation-correction iterations are not needed (Fig. 11(a)). Nevertheless, an output can be outside the specified tolerance because of stochastic fluctuations. In this simulation, only the kMC output θ_B changes due to its dependency on the applied sinusoidal current input. Therefore, θ_B is most critical and its progress over the iterations is shown in detail in Fig. 11(b). Within one sequence, the estimated value approaches the actual value until it is within the specified tolerance. The number of iterations needed can considerably deviate between sequences. The probability that one of the evaluated parameters is outside the specified tolerance because of stochastic fluctuations increases with the number of evaluated parameters. As the algorithm needs to hold all the selected output parameters within the specified tolerance, convergence can be challenging when having more than one interdependent output. The problem as a whole is similar to a robust control problem (Rusli et al., 2004).

Fig. 12 shows convergence of the critical variable θ_B for varying simulation parameters. Increasing the field size decreases the fluctuations of the kMC output (cf. Figs. 11(b) and 12(a)), which decreases the output uncertainty and in general should help to control to the tolerance range. However, as tolerance is defined as a function of standard deviation, as given with Eq. (43), the total number of iterations increased to almost 600 iterations. Moreover, the computational cost of a single iteration significantly in-

Fig. 12. Convergence behavior for the kMC output θ_B for variations of the algorithm parameter set: (a) increased field size, (b) increased proportional factor, and (c) decreased tolerance factor.

creases due to increased number of grid elements, resulting in a total computational time of 42,011 s instead of 8046 s. This factor of five increase in computational cost only produces a slightly improved accuracy (Fig. 10(a)). As discussed in the previous section, the overall error of the solution cannot be reduced below the transition error, which is not affected by increasing the field size. Further increasing the field size will thus not further reduce the error of θ_B. Considering the significantly increased computational cost, the slight improvement of accuracy is not worth the effort for this example.

Increasing the proportional factor K_P from 0.2 to 0.8 gives faster convergence (Fig. 12(b)), with a considerable reduction of the number of iterations compared to the reference configuration. Drawbacks of the higher proportional factor are overshooting and oscillation of the estimation. A systematic optimization of K_P and K_I would lead to a faster convergence without oscillation, i.e. a further reduction of the number of iterations and computational cost.

Decreasing the tolerance factor λ from 1 to 0.75 increases the number of iterations increases significantly, from 450 to more than 800 iterations (Fig. 12(c)). In several sequences, the estimation reaches a steady value, but the tolerance region is not reached, which suggests that the chosen tolerance is too low compared to the fluctuation of the kMC output. Although the estimation is good, the kMC output variables are often outside the tolerance region. One option for reducing the iterations is to define the tolerance according to the standard deviation or higher.

4. Conclusions

This article presents a systematic analysis of coupling algorithms for the multiscale simulation of surface processes for electrochemical systems. Any of three presented algorithms can be a good choice for multiparadigm simulation, depending on the needs and tradeoffs in numerical accuracy and computational cost. The coupling algorithms without estimation-correction were more than an order-of-magnitude less computationally expensive, but also an order-of-magnitude less accurate. Errors in the coupled simulations originate from several different causes and are categorized into fluctuation, prediction, and transition errors. Measures that are efficient in reducing one error type may be futile or even counterproductive regarding the other error types. Quantitative analysis as done in this study should be carried out to learn the underlying causes of numerical errors to facilitate an efficient and robust design of the coupling algorithm. While computationally efficient algorithms such as MPA1 and MPA2 can be suitable for some applications, the sequence size length needs to be considered carefully to keep fluctuation errors and sequence size-dependent errors in the same order of magnitude. Algorithms that include estimation-correction, such as MPA3, are much more robust regarding configuration and possess the highest accuracy for all configurations evaluated here.

To conclude, this work analyzes coupling algorithms applicable for multiscale simulations in electrochemical systems. This article provides a guide for the systematic selection and design of compu-

tationally efficient and accurate coupling simulations. One of the observations made in this article is that the tuning of the coupling parameters is not as straightforward as in most simulation algorithms. For example, increasing a simulation parameter such as the number of sequences may lead to an order of magnitude reduction in the average errors for some variables while simultaneously leading to an order of magnitude increase in average errors for other variables (cf. Fig. 8(f) and (i)). This behavior is in contrast to the simulation of an ordinary differential equation (ODE), in which increasing the number of sequences within a fixed time interval is generally considered a reliable approach for reducing average errors for all variables in the ODE. By taking into account the findings of this work, inappropriate or inefficient multiscale simulations can be prevented. Thus the article significantly contributes to the establishment of multiscale simulation techniques for simulation of electrochemical systems and heterogeneous catalysis.

Acknowledgments

References

Andreaus, B., Eikerling, M., 2007. Active site model for CO adlayer electrooxidation on nanoparticle catalysts. J. Electroanalytical Chem. 607, 121–132.

Blanquer, G., Yin, Y., Quiroga, M.A., Franco, A.A., 2016. Modeling investigation of the local electrochemistry in lithium-o_2 batteries: a kinetic Monte Carlo approach. J. Electrochem. Soc. 163 (3), 329–337.

Braatz, R.D., Alkire, R.C., Seebauer, E., Rusli, E., Gunawan, R., Drews, T.O., Li, X., He, Y., 2006. Perspectives on the design and control of multiscale systems. J. Process Control 16 (3), 193–204.

Braatz, R.D., Alkire, R.C., Seebauer, E.G., 2008. Multiscale modeling and design of electrochemical systems. In: Alkire, R.C., Kolb, D.M., Lipkowski, J., Ross, P.N. (Eds.), Electrochemical Surface Modification – Thin Films, Functionalization and Characterization. In: Advances in Electrochemical Science and Engineering, 10. Wiley-VCH, Weinheim, Germany, pp. 298–334.

Burghaus, U. (Ed.), 2006. A Practical Guide to Kinetic Monte Carlo Simulations and Classical Molecular Dynamics Simulations: An Example Book. Nova Science Publ., New York.

Drews, T.O., Radisic, A., Erlebacher, J., Braatz, R.D., Searson, P.C., Alkire, R.C., 2006. Stochastic simulation of the early stages of kinetically limited electrodeposition. J. Electrochem. Soc. 153, C434–C441.

Drews, T.O., Webb, E.G., Ma, D.L., Alameda, J., Braatz, R.D., Alkire, R.C., 2004. Coupled mesoscale-continuum simulations of copper electrodeposition in a trench. AIChE J. 50 (1), 226–240.

Franco, A.A., 2013. Multiscale modelling and numerical simulation of rechargeable lithium ion batteries: concepts, methods and challenges. RSC Adv. 3, 13027–13058.

Goldin, G., Zhu, H., Kattke, K., Dean, A., Braun, R., Kee, R.J., Zhang, D., Maier, L., Deutschmann, O., 2009. Coupling complex reformer chemical kinetics with three-dimensional computational fluid dynamics. ECS Trans. 25 (2), 1253–1262.

Jahnke, T., Futter, G., Latz, A., Malkow, T., Papakonstantinou, G., Tsotridis, G., Schott, P., Gérard, M., Quinaud, M., Quiroga, M., Franco, A.A., Malek, K., Calle–Vallejo, F., Ferreira De Morais, R., Kerber, T., Sautet, P., Loffreda, D., Strahl, S., Serra, M., Polverino, P., Pianese, C., Mayur, M., Bessler, W.G., Kompis, C., 2016. Performance and degradation of proton exchange membrane fuel cells: state of the art in modeling from atomistic to system scale. J. Power Sources 304, 207–233.

Kalz, K.F., Kraehnert, R., Dvoyashkin, M., Dittmeyer, R., Gläser, R., Krewer, U., Reuter, K., Grunwaldt, J.-d., 2016. Future challenges in heterogeneous catalysis: understanding catalysts under dynamic reaction conditions. Chem. Cat. Chem. 9, 1–14.

Lin, N., Xie, X., Schenkendorf, R., Krewer, U., 2018. Efficient global sensitivity analysis of 3d multiphysics model for li-ion batteries. J. Electrochem. Soc. 165 (7), A1169–A1183.

Madec, L., Falk, L., Plasari, E., 2001. Simulation of agglomeration reactors via a coupled CFD/direct Monte-Carlo method. Chem. Eng. Sci. 56, 1731–1736.

Matera, S., Maestri, M., Cuoci, A., Reuter, K., 2014. Predictive-quality surface reaction chemistry in real reactor models: integrating first-principles kinetic Monte Carlo simulations into computational fluid dynamics. ACS Catal. 4 (11), 4081–4092. doi:10.1021/cs501154e.

Methekar, R.N., Northrop, P.W.C., Chen, K., Braatz, R.D., Subramanian, V.R., 2011. Kinetic Monte Carlo simulation of surface heterogeneity in graphite anodes for lithium-Ion batteries: passive layer formation. J. Electrochem. Soc. 158 (4), A363–A370.

Pal, S., Landau, D.P., 1994. Monte Carlo simulation and dynamic scaling of surfaces in MBE growth. Phys. Rev. B 49 (15), 10597–10606.

Pornprasertsuk, R., Cheng, J., Huang, H., Prinz, F.B., 2007. Electrochemical impedance analysis of solid oxide fuel cell electrolyte using kinetic Monte Carlo technique. Solid State Ionics 178 (3–4), 195–205.

Quiroga, M.A., Franco, A.A., 2015. A multi-paradigm computational model of materials electrochemical reactivity for energy conversion and storage. J. Electrochem. Soc. 162 (7), E73–E83.

Quiroga, M.A., Malek, K., Franco, A.A., 2016. A multiparadigm modeling investigation of membrane chemical degradation in PEM fuel cells. J. Electrochem. Soc. 163 (2), F59–F70.

Ramadesigan, V., Northrop, P.W.C., De, S., Santhanagopalan, S., Braatz, R.D., Subramanian, V.R., 2012. Modeling and simulation of lithium-ion batteries from a systems engineering perspective. J. Electrochem. Soc. 159, R31–R45.

Reuter, K., 2011. First-Principles Kinetic Monte Carlo Simulations for Heterogeneous Catalysis: Concepts, Status, and Frontiers. Wiley-VCH Verlag GmbH & Co. KGaA, pp. 71–111.

Ricardez-Sandoval, L.A., 2011. Current challenges in the design and control of multiscale systems. Can. J. Chem. Eng. 89, 1324–1341.

Röder, F., Braatz, R.D., Krewer, U., 2017. Multi-scale simulation of heterogeneous surface film growth mechanisms in lithium-ion batteries. J. Electrochem. Soc. 164 (11), E3335–E3344.

Rusli, E., Drews, T.O., Braatz, R.D., 2004. Systems analysis and design of dynamically coupled multiscale reactor simulation codes. Chem. Eng. Sci. 59, 5607–5613.

Salciccioli, M., Stamatakis, M., Caratzoulas, S., Vlachos, D.G., 2011. A review of multiscale modeling of metal-catalyzed reactions: mechanism development for complexity and emergent behavior. Chem. Eng. Sci. 66 (19), 4319–4355.

To, A.C., Li, S., 2005. Perfectly matched multiscale simulations. Phys. Rev. B 72, 035414.

Vlachos, D., 1997. Multiscale integration hybrid algorithms for homogeneous-heterogeneous reactors. AIChE J. 43 (11), 3031–3041.

Weinan, E., Engquist, B., Huang, Z., 2003. Heterogeneous multiscale method: a general methodology for multiscale modeling. Phys. Rev. B 67, 092101.

Zheng, Z., Stephens, R.M., Braatz, R.D., Alkire, R.C., Petzold, L.R., 2008. A hybrid multiscale kinetic Monte Carlo method for simulation of copper electrodeposition. J. Comput. Phys. 227 (10), 5184–5199.